






Ring Bose-Einstein condensate in a cavity: Chirality detection and rotation sensingNalinikanta Pradhan ¹, Pardeep Kumar ^{2,*}, Rina Kanamoto ³, Tarak Nath Dey ¹,
M. Bhattacharya ⁴ and Pankaj Kumar Mishra¹¹*Department of Physics, Indian Institute of Technology, Guwahati 781039, Assam, India*²*Max Planck Institute for the Science of Light, Staudtstraße 2, 91058 Erlangen, Germany*³*Department of Physics, Meiji University, Kawasaki, Kanagawa 214-8571, Japan*⁴*School of Physics and Astronomy, Rochester Institute of Technology, 84 Lomb Memorial Drive, Rochester, New York 14623, USA*

(Received 26 November 2023; accepted 26 January 2024; published 21 February 2024)

Recently, a method has been proposed to detect the rotation of a ring Bose-Einstein condensate, *in situ*, in real-time, and with minimal destruction by using a cavity driven with optical fields carrying orbital angular momentum [Phys. Rev. Lett. **127**, 113601 (2021)]. This method is sensitive to the magnitude of the condensate winding number but not its sign. In the present work, we consider simulations of the rotation of the angular lattice formed by the optical fields and show that the resulting cavity transmission spectra are sensitive to the sign of the condensate winding number. We demonstrate the minimally destructive technique on persistent current rotational eigenstates, counter-rotating superpositions, and a soliton singly or in collision with a second soliton. Conversely, we also investigate the sensitivity of the ring condensate, given knowledge of its winding number, to the rotation of the optical lattice. This characterizes the effectiveness of the optomechanical configuration as a laboratory rotation sensor. Our results are important to studies of rotating ring condensates used in atomtronics, superfluid hydrodynamics, simulation of topological defects and cosmological theories, interferometry using matter-wave solitons, and optomechanical sensing.

DOI: [10.1103/PhysRevA.109.023524](https://doi.org/10.1103/PhysRevA.109.023524)**I. INTRODUCTION**

Degenerate atoms contained in a ring-shaped potential are paradigms of quantum rotation [1–5]. Specifically, a Bose-Einstein condensate (BEC) in a ring displays quantized persistent superflow [6], phase slips [7,8], solitons [9], hysteresis [10,11], excitations [12], spinor hydrodynamics [13,14], and shock waves [15]. Such a BEC can be used to simulate topological systems [16–18], black holes [19], the early universe [20], and time crystals [21]. Apart from fundamental interest, ring BECs are platforms critical to applications such as matter-wave interferometry [22,23], gyroscopy [24,25], atomtronics [26–29], quantum computation [30], and rotation sensing [31].

In all of the investigations mentioned above, a central role is played by the state of rotation of the condensate. It is no surprise that therefore a number of methods exist for probing the condensate winding number, or topological charge, which is the angular momentum per atom divided by Planck's constant \hbar . In the earliest instances, the method involved measuring the diameter of the central density hole of the atomic distribution upon time-of-flight expansion and subsequent absorption

imaging [13,32]. This diameter is proportional to the magnitude of the initial condensate vortex charge. However, the method does not yield the sign of the winding number, which is the direction of the atomic rotation. Another technique, which provides the same information, involves interferometric processing of the condensate so that the image contains a number of density peaks equal in number to the winding number [6].

Subsequently, methods that revealed the sign of the winding number were demonstrated. One way of implementing such detection is to use a disk-shaped reference condensate, which is also allowed (along with the ring) to expand via time-of-flight and the matter-wave phase interferogram resulting from its interference with the ring carries a clear signature of the handedness of the atomic rotation. Specifically, if the ring is not rotating, the interferogram fringes consist of a set of concentric circles. If the ring is rotating, the fringes appear in the shape of nested spirals whose number and handedness reveal the magnitude and sign, respectively, of the condensate winding number [18].

However, all demonstrated methods of detecting ring BEC rotation are fully destructive of the condensate because they all employ absorption imaging [33]. The absorption and subsequent emission of photons destroy the coherence of the atomic condensate. In recent work, our group proposed a method for detecting atomic rotation with minimal destruction to the condensate in real-time and *in situ* [34,35]. Our proposal involved coupling the rotating ring BEC to a resonator using optical beams carrying orbital angular momentum (OAM) [see Fig. 1] and subsequently carrying out a homodyne detection of the phase quadrature of the cavity output field using

*pardeep.kumar@mpl.mpg.de

Published by the American Physical Society under the terms of the Creative Commons Attribution 4.0 International license. Further distribution of this work must maintain attribution to the author(s) and the published article's title, journal citation, and DOI. Open access publication funded by the Max Planck Society.

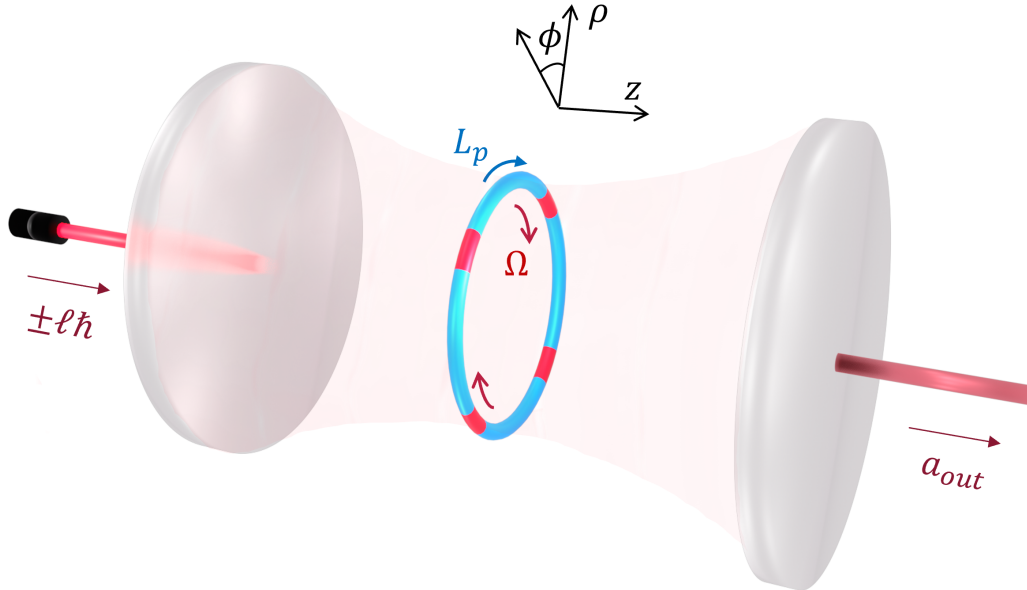


FIG. 1. Schematic illustration of a Bose-Einstein condensate with winding number L_p trapped in a ring. Two Laguerre-Gauss cavity modes carrying orbital angular momenta $\pm \ell \hbar$ form an annular lattice to probe the dynamics of the condensate. The lattice is rotated at frequency Ω . The optical field transmitted by the cavity is denoted by a_{out} .

the well-established detection techniques of cavity optomechanics [36–38]. The signal was shown to contain two peaks, from the frequency location of either of which the condensate winding number could be inferred. While the initial proposal modeled the BEC as a two-mode system, in subsequent work we used a mean-field model that accounts for all the matter wave modes of the BEC and considered persistent currents as well as solitons [35].

Nevertheless, the minimally destructive technique proposed by us only reveals the magnitude, and not the sign of the winding number, of the ring BEC. This may be understood from a symmetry point of view by realizing that the optical beams introduced by us produce an angular lattice overlapping with the ring BEC (see Fig. 1). Since this lattice breaks rotational symmetry about the cavity axis, it can probe the angular momentum, i.e., the winding number, of the condensate. However, since it does not break chiral symmetry by picking a handedness about the cavity axis, it is insensitive to the sign of the condensate rotation.

In the present work, we show that the rotation of the optical lattice, which can be carried out in the laboratory using spatial light modulators [39], allows us to determine the sign of the condensate rotation. For realistic lattice rotation frequencies, we demonstrate our technique on persistent current rotational eigenstates and counter-rotating superpositions for weak and repulsive atomic interactions. We also show how the method works for solitons, singly or in colliding pairs, for weak and attractive atomic interactions [40–47]. Finally, we also consider the converse of the problem, where we think of the lattice rotation as caused by the laboratory and ask how well a condensate with a known winding number can measure this rotation. In other words, we consider the sensitivity of the ring BEC in a cavity as a rotation sensor.

We present analytical few-mode calculations, where possible, and numerical simulations that treat the condensate in the mean-field limit and the cavity field classically. Damping and

noise arising from the matter as well as optical fields are modeled realistically. Our results include the homodyne spectra of the cavity transmission [37], which establish the sign as well as magnitude of the condensate rotation, the sensitivity of the measurement as a function of system response frequency, and atomic density profiles showing the effect of the measurement on the condensate. Before concluding, we mention that a theoretical proposal for measuring the magnitude as well as the sign of the condensate winding number using atom counting exists [48].

This paper is organized as follows: In Sec. II the theoretical model and details of the numerical simulation are presented. In Secs. III A and III B we provide the dynamics, OAM content, optical spectra, and measurement sensitivity for persistent current and bright soliton detection, respectively. In Sec. III C we present a detailed analysis of the critical rotation required for using the ring BEC as a rotation sensor. Following this, the fidelity is presented in Sec. III D. Finally, we conclude our work in Sec. IV. In the Appendix B, we present the BEC chirality detection and rotation sensing at high lattice rotation frequencies.

II. THEORETICAL MODEL AND DETAILS OF NUMERICAL SIMULATION

In this section, we describe the few-mode quantum-mechanical model for the configuration of interest and the mean-field equations, which take all modes of the condensate into account.

A. Few-mode Hamiltonian

We consider a BEC confined in a ring trap of radius R , whose center lies on the axis of an optical resonator; see Fig. 1. The BEC is probed by a superposition of frequency-degenerate Laguerre-Gaussian beams carrying

optical OAM $\pm \ell \hbar$. The combination of these beams creates an angular lattice inside the cavity, overlapping with the ring BEC. The matter waves in the condensate Bragg diffract from this lattice, giving rise to persistent current side modes $L_p \rightarrow L_p \pm 2\ell$, where L_p is the winding number of the supercurrent initially present in the BEC.

In the rotating frame of the laser drive and the rest frame of the optical lattice, the azimuthal dynamics of the BEC are described in terms of the Hamiltonian written in second-quantized form:

$$\begin{aligned} \hat{H}_0 = & \int_0^{2\pi} \Psi^\dagger(\phi) \left[\left(-i \frac{d}{d\phi} \right)^2 + U_0 \cos^2(\ell\phi) a^\dagger a \right] \Psi(\phi) d\phi \\ & + \frac{\mathcal{G}}{2} \int_0^{2\pi} \Psi^\dagger(\phi) \Psi^\dagger(\phi) \Psi(\phi) \Psi(\phi) d\phi \\ & - \Delta_o a^\dagger a - i\eta(a - a^\dagger), \end{aligned} \quad (1)$$

where $\Psi(\phi)$ is the bosonic atomic field operator such that $[\Psi(\phi), \Psi^\dagger(\phi')] = \delta(\phi - \phi')$, and ϕ is the angular variable of atomic position along the ring. The optical field operators, on the other hand, obey $[a, a^\dagger] = 1$. The square bracket in the first line of Eq. (1) has two terms: (i) the first term represents the rotational kinetic energy of the atoms, and (ii) the second contribution governs the interaction of the atoms with the optical lattice potential such that $U_0 = g_0^2/\Delta_a$, where g_0 and Δ_a are the single photon-atom coupling strength and detuning of the optical drive from the atomic transition, respectively. The two-body atomic interaction with the strength $\mathcal{G} = g/\hbar\omega_\beta$ is represented in the second line of Eq. (1) which corresponds to binary collisions in the condensate. Here $g = 2\hbar\omega_\rho a_s/R$ depends on the atomic s -wave scattering length a_s and the harmonic trap frequency along the radial direction ω_ρ ; further, ω_β is defined to scale the energy such that $\hbar\omega_\beta = \hbar^2/(2mR^2)$, where m is the atomic mass. The terms in the last line of Eq. (1) contain contributions from the cavity field energy and the cavity drive, respectively. Here Δ_o is the drive detuning from the cavity resonance ω_o and $\eta = \sqrt{P_{\text{in}}\gamma_o/\hbar\omega_o}$ is the drive strength, where P_{in} (γ_o) is the input optical power (cavity linewidth).

B. Rotating angular lattice

As the angular lattice breaks the rotational symmetry of the system about the cavity axis, it can be used to probe the winding number L_p of the ring condensate. However, the lattice does not break the chiral symmetry of the system by providing a preferred handedness, and only the magnitude of L_p can be found using this method, as shown earlier [34].

To detect the *sign* of the persistent current, we break the chiral symmetry of the system by rotating the optical lattice with an angular frequency of Ω [39,49,50]. Mathematically, this corresponds to replacing $\cos^2(\ell\phi)$ on the first line of Eq. (1) by $\cos^2[\ell(\phi + \Omega t)]$. Using then the operator $e^{i\Omega L_\phi t}$ that transforms the Hamiltonian from the laboratory to the rotating frame of the optical angular lattice, where

$$\hat{L}_\phi = \int_0^{2\pi} \Psi^\dagger(\phi) \left(-i \frac{d}{d\phi} \right) \Psi(\phi) d\phi. \quad (2)$$

is the angular-momentum operator, we obtain

$$\hat{H}(\Omega) = \hat{H}_0 - \Omega \hat{L}_\phi. \quad (3)$$

Using Eqs. (1) and (2) in Eq. (3) and adding the constant terms, the Hamiltonian in the rotating optical lattice frame becomes [9]

$$\begin{aligned} \hat{H}(\Omega) = & \int_0^{2\pi} \Psi^\dagger(\phi) \left[\left(-i \frac{d}{d\phi} - \frac{\Omega}{2} \right)^2 \right] \Psi(\phi) d\phi \\ & + \int_0^{2\pi} \Psi^\dagger(\phi) U_0 \cos^2(\ell\phi) a^\dagger a \Psi(\phi) d\phi \\ & + \frac{\mathcal{G}}{2} \int_0^{2\pi} \Psi^\dagger(\phi) \Psi^\dagger(\phi) \Psi(\phi) \Psi(\phi) d\phi \\ & - \Delta_o a^\dagger a - i\eta(a - a^\dagger). \end{aligned} \quad (4)$$

Physically, the atoms of the condensate get Bragg diffracted from the optical lattice. We consider photon numbers smaller than unity in the cavity (this has already been achieved experimentally [36,51]); hence, the lattice is weak, and only first-order atomic diffraction is non-negligible. This results in two side modes, ω_c and ω_d , respectively, in terms of the matter-wave OAM states. The frequencies of these side modes can be deduced by following the procedure outlined in Ref. [34], with a straightforward modification arising from the transformation between laboratory and lattice rotation frames

$$\omega_{c,d}(\Omega) = \omega_\beta \left(L_p \pm 2\ell - \frac{\Omega'}{2} \right)^2, \quad (5)$$

where the normalized angular frequency is $\Omega' = \Omega/\omega_\beta$. From Eq. (5) it follows that, for a fixed angular frequency Ω' of lattice rotation, the frequencies of the side modes are different for opposite winding numbers $\pm L_p$. Thus, this technique can be used to infer the direction of the BEC rotation. In contrast, in the absence of lattice rotation ($\Omega' = 0$), it can be verified that transforming $L_p \leftrightarrow -L_p$ merely exchanges the side mode frequencies ($\omega_c \leftrightarrow \omega_d$), thus leaving the sign undetermined. In the above discussion, we have neglected the effect of atomic interactions on the side mode frequencies. Inclusion of interactions leads to the modified frequencies [9,34]

$$\omega'_{c,d} = [\omega_{c,d}(\omega_{c,d} + 4\tilde{g}N)]^{1/2}, \quad (6)$$

where $\tilde{g} = g/(4\pi\hbar)$ and N is the number of atoms in the condensate. We compare the analytical expression of the side mode frequencies from Eqs. (6) to our numerical simulations presented below. In the simulations, we calculate the noise spectrum of the phase quadrature a_{out} of the field transmitted by the cavity, see Fig. 1. Experimentally, this corresponds to the homodyne measurement of the cavity output field a_{out} with respect to the local oscillator supplied by the input field a_{in} [37].

We note that the optical lattice rotates through the condensate, presenting obstacles that are penetrable by the superfluid, since the peak optical potential $U_0|\alpha_s|^2$ (where $|\alpha_s|^2$ is the steady-state photon number in the cavity) is always smaller than the chemical potential μ . In this work, we only consider lattice rotation rates smaller than the speed of sound $v_s = \sqrt{\mu/m}$ in the condensate, i.e., such that $\omega_\beta\Omega' < v_s/(2\pi R)$. This ensures that the flow around the ring is always

superfluidic, and the local Landau criterion for the onset of dissipative flow is never satisfied [52].

C. Equations of motion

In contrast with the few-mode model discussed above, we now take into account the full-mode characterization of the condensate by employing a mean-field Gross–Pitaevskii formalism. Using Eqs. (4), the mean-field equation can be derived, including the fluctuations [53,54]. Then the coupled dynamical equations for the condensate wave function ψ and light field amplitude α in the rotating optical lattice are written as [35]

$$(i - \Gamma) \frac{d\psi}{d\tau} = \left[-\frac{d^2}{d\phi^2} + \frac{U_0}{\omega_\beta} |\alpha(\tau)|^2 \cos^2(\ell\phi) - \mu + \mathcal{G}|\psi|^2 - \Omega' \left(-i \frac{d}{d\phi} \right) \right] \psi + \xi(\phi, \tau), \quad (7)$$

and

$$i \frac{d\alpha}{d\tau} = \left\{ -\left[\Delta_c - U_0 \langle \cos^2(\ell\phi) \rangle_\tau + i \frac{\gamma_0}{2} \right] \alpha + i\eta \right\} \alpha + i\sqrt{\gamma_0} \omega_\beta^{-1} \alpha_{\text{in}}(\tau). \quad (8)$$

Equation (7) is the dimensionless stochastic Gross–Pitaevskii equation, where $\psi \equiv \psi(\phi, \tau)$ represents the condensate wave function, which is normalized to the total number of atoms in the condensate N , as expressed by

$$\int_0^{2\pi} |\psi(\phi, \tau)|^2 d\phi = N. \quad (9)$$

Here ϕ and τ are the angular coordinates along the ring and the scaled time respectively. The length is normalized to the radius of the ring R , while the energy and time are normalized as $\hbar\omega_\beta = \hbar^2/2mR^2$ and $\tau = \omega_\beta t$, respectively. Since most of the terms used in Eqs. (7) and (8) have been described in earlier sections, only a brief discussion of the terms associated with the fluctuations is presented here. The optical fluctuation is taken into account through the term $\alpha_{\text{in}}(\tau)$ and the thermal fluctuation associated with the condensate is through $\xi(\phi, \tau)$, which is related to the damping of the condensate Γ (scaled with ω_β) according to the fluctuation-dissipation theory [55] and to conserve the norm of the condensate in presence of this fluctuation, the chemical potential μ is corrected at each time step as [56]

$$\Delta\mu = (\Delta\tau)^{-1} \ln \left[\frac{\int |\psi(\phi, \tau)|^2 d\phi}{\int |\psi(\phi, \tau + \Delta\tau)|^2 d\phi} \right].$$

Here both the thermal and optical noise are considered to be delta-correlated white noise, with the correlations [17,34,35]

$$\langle \xi(\phi, \tau) \xi^*(\phi', \tau') \rangle = \frac{2\Gamma k_B T}{\hbar\omega_\beta} \delta(\phi - \phi') \delta(\tau - \tau'), \quad (10)$$

$$\langle \alpha_{\text{in}}(\tau) \alpha_{\text{in}}^*(\tau') \rangle = \omega_\beta \delta(\tau - \tau'). \quad (11)$$

So the terms $\xi(\phi, \tau)$ and $\alpha_{\text{in}}(\tau)$ can be modeled as

$$\xi(\phi, \tau) = \sqrt{\frac{2\Gamma k_B T}{\hbar\omega_\beta d\phi d\tau}} \mathcal{N}(0, 1, N_\phi) \mathcal{N}(0, 1, N_\phi), \quad (12)$$

$$\alpha_{\text{in}}(\tau) = \sqrt{\omega_\beta/d\tau} \mathcal{N}(0, 1, 1), \quad (13)$$

where k_B is the Boltzmann constant and T is the temperature of the bath. Here $\mathcal{N}(0, 1, N_\phi)$ and $\mathcal{N}(0, 1, 1)$ are the sets of random variables that are normally distributed, having zero mean and unit variance. The third argument in \mathcal{N} denotes the size of the array, containing the random numbers that are added in each time step with the prefactor while solving the above-mentioned coupled differential equations. Additional discussions of the measurement noise including the quantum backaction have been provided in the Appendix A.

D. Simulation details

In this work, we have considered four different states of the condensate, namely, persistent current, superposition state, soliton, and two-soliton states moving with equal and opposite angular velocity. First, in Sec. III A, we demonstrate the dynamics of a single persistent current and two counterpropagating persistent currents in a superpositioned state. Subsequently, in Sec. III B, we present the dynamics of a bright soliton and the dynamics of a pair of solitons that undergo multiple collisions. The dynamics of the persistent current are captured by solving the coupled set of dynamical equations [Eqs. (7) and (8)] numerically using the real-time dynamics scheme. We use the Fourier pseudospectral method [57] aided by the fourth-order Runge-Kutta scheme for the temporal evolution of the condensate [58]. For persistent current, we start the simulation by considering the initial state as $e^{iL_p\phi}$. However, to generate a soliton-like ground state, we first evolve the condensate with the Gaussian state $e^{-\phi^2/2}$, which resembles the shape of a bright soliton, using the imaginary time scheme based upon the Strang splitting Fourier method [59]. Subsequently, the soliton initial state is modulated with a phase $e^{iL_p\phi}$ to achieve the moving soliton state, which is further evolved using the real-time scheme.

For all the simulation runs, the dynamics of condensate and cavity are captured for a period of 5 s that gives a single trajectory of the cavity field, which is later used to obtain the cavity output spectrum through a Fourier transformation. From these results, we can also obtain t_{meas} , the time required for the measurement, and verify that it is much smaller than any relevant dynamical timescale in the problem, and thus conclude that the measurement is practically in real time. For enhanced visualization, the cavity output spectrum is smoothed using the moving average technique of a window size of 30 Hz. The rotation measurement sensitivities have been calculated by fitting the output spectrum near the frequency at which we get the peaks with the appropriate shape. This process allows us to reduce the effect of background noise coming from the frequency away from the relevant ones in the calculation of the sensitivity. For all the simulation runs, we have chosen the dt as 10^{-7} where the space resolution $d\phi$ is set at 0.006.

III. RESULTS AND DISCUSSION

A. Persistent current

1. Rotational eigenstate

We consider a condensate comprised of N number of ^{23}Na atoms [1] each of mass m , confined in an annular trap generating a persistent current. Since the configuration we are proposing has not yet been realized, we take parameters for

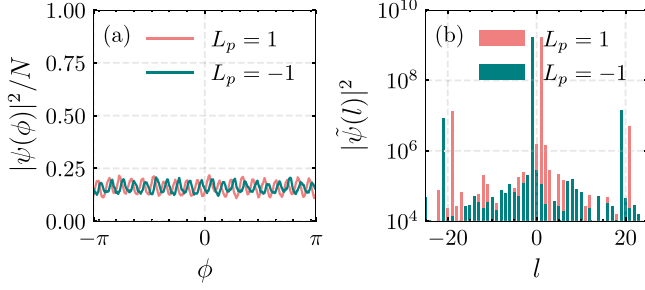


FIG. 2. Persistent current: (a) angular profile of the condensate density per particle for a persistent current rotational eigenstate. (b) OAM state content of the condensate. Parameters used here are $\Omega' = 0.5$, $L_p = \pm 1$, $\Gamma = 0.0001$, $T = 10$ nK, $g/\hbar \simeq 2\pi \times 0.02$ Hz, $\ell = 10$, $N = 10^4$, $\tilde{\Delta} = -2\pi \times 173$ Hz, $U_0 = 2\pi \times 212$ Hz, $\gamma_0 = 2\pi \times 2$ MHz, $P_{\text{in}} = 50$ fW, $\Omega' = 0.5$, $\omega_c = 2\pi \times 10^{15}$ Hz, $m = 23$ amu, and $R = 12$ μm .

our simulations from a combination of experiments: on BECs in cavities [36], ring BECs independent of cavities [1,7], and OAM modes in cavities [60]. The initial macroscopic condensate wave function, representing the rotational state of persistent current, can be assumed to have the form of a plane wave,

$$\psi(\phi) = \sqrt{\frac{N}{2\pi}} e^{iL_p\phi}. \quad (14)$$

Here $e^{iL_p\phi}$ is the phase factor, which presents a phase gradient to the condensate of uniform density, and L_p represents the winding number of the condensate, which is the quantity to be detected.

As our present method can detect the magnitude as well as the sign of the winding number of the persistent current, in this section, we present the simulation results for two different currents having winding numbers $\pm L_p$ for specific values of the angular frequency of the rotating optical lattice Ω' . In Fig. 2 we show the ground-state density profiles obtained for $L_p = \pm 1$ with the rotation frequency $\Omega' = 0.5$, along with the occupation of matter wave OAM states for both these values of L_p . We emphasize that our minimally destructive measurement does not yield condensate density or OAM content—these can only be obtained from a fully destructive measurement. They have been provided here as they can be simulated and provide a more complete description of the measurement.

We find that the condensate density profiles are quite similar to each other and appear to be slightly modulated as a result of the rotating optical lattice and the noise present in the system [see Fig. 2(a)]. To illustrate the presence of different matter wave OAM modes, we show the Fourier transformation of the density of the persistent currents in frequency space corresponding to $L_p = \pm 1$ in Fig. 2(b). Here, the side modes at the position $L_p \pm 2l - \Omega'/2$ appear due to matter-wave diffraction.

To probe the different OAM components present in the condensate, we compute the spectrum of the output optical field, which is transmitted through the cavity. Within the cavity, the light field is modulated at the side mode frequencies of the condensate $\omega'_{c,d}(\Omega)$, Eq. (6) [34,36]. To reveal these

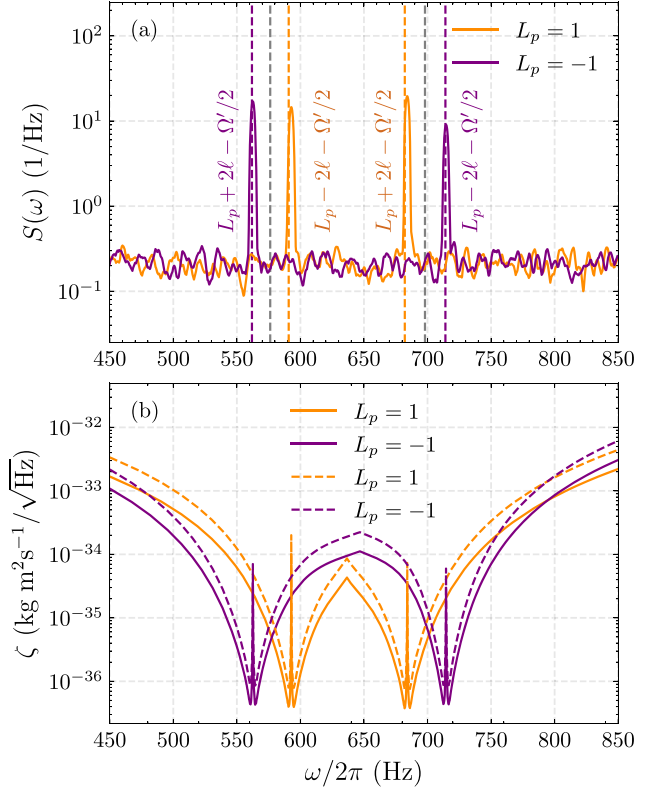


FIG. 3. Persistent current: (a) Noise spectra of the output phase quadrature of the cavity field and (b) rotation measurement sensitivity versus the system response frequency for different winding numbers $L_p = \pm 1$. In panel (a), the gray-colored vertical dashed line corresponds to the analytical predictions for the side modes for $\Omega' = 0$ (provided as a reference to indicate the opposite direction of shifts for $L_p = \pm 1$) and the orange and purple-colored vertical dashed lines correspond to the analytical predictions for the side modes for $\Omega' = 0.5$. In panel (b), the solid curves correspond to ζ^Δ [Eq. (16)], while the dashed curves correspond to ζ^Ω [Eq. (17)]. Here $G = 2\pi \times 7.5$ kHz, $|\alpha_s|^2 = 0.024$, and the optomechanical measurement time (t_{meas}) is 9.4 ms. The other parameters used here are the same as mentioned in Fig. 2.

side mode frequencies, we perform a Fourier transform of the cavity field amplitude of the output field, which is related to the intracavity field through the input-output relation of cavity optomechanics as $\alpha_{\text{out}} = -\alpha_{\text{in}} + \sqrt{\gamma_0}\alpha$ [37]. For all the analysis performed in the paper, we consider the phase quadrature of the cavity transmission spectrum defined as

$$S(\omega) = |\text{Im}[\alpha_{\text{out}}(\omega)]|^2. \quad (15)$$

Experimentally, this spectrum can be obtained via a homodyne measurement of the cavity output with respect to the local oscillator of the cavity input. Figure 3(a) depicts the phase quadrature of the cavity transmission spectrum as a function of the response frequency of the system for two different situations (the same as in Fig. 2), i.e., for the winding numbers $L_p = \pm 1$. The spectrum clearly shows two distinct peaks at the locations corresponding to the side mode frequencies $\omega'_{c,d}(\Omega)$ for $L_p = \pm 1$. The numerically simulated peak positions match quite well with the analytical predictions of Eq. (6).

Next, we compute the sensitivity of detecting L_p for a fixed value of angular frequency of rotating optical lattice Ω' , defined as

$$\zeta^\Lambda = \frac{S(\omega)}{\partial S(\omega)/\partial \Lambda} \sqrt{t_{\text{meas}}}, \quad (16)$$

and also the sensitivity of measuring the rotation of the optical lattice Ω for a fixed value of L_p defined as

$$\zeta^\Omega = \frac{S(\omega)}{\partial S(\omega)/\partial (\hbar\Omega')} \sqrt{t_{\text{meas}}}. \quad (17)$$

Here $t_{\text{meas}}^{-1} = 8(\alpha_s G)^2/\gamma_0$ is the optomechanical measurement rate, $G = U_0\sqrt{N}/2\sqrt{2}$ [34], and $\Lambda = \hbar L_p$ is the angular momentum of the condensate. In Fig. 3(b), we show the sensitivities ζ^Ω and ζ^Λ , respectively, as functions of the system rotation frequency. The sensitivities of detecting the condensate winding number L_p and rotation of the optical lattice Ω are optimized near the side mode frequencies $\omega'_{c,d}(\Omega)$. For the detection of L_p the optimal sensitivities of $\approx 10^{-37}$ kg m² s⁻¹ Hz^{-1/2} compare well with our earlier work [34], indicating also that all relevant sources of noise have been accounted for.

To demonstrate that our method is effective at detecting two neighboring winding numbers, we further compute the cavity output spectrum for $L_p = \pm 2$ as shown in Fig. 4(a), where the peaks are spectrally distinct from the peaks for the case of $L_p = \pm 1$ [Fig. 3(a)]. The corresponding sensitivities of measurement are illustrated in Fig. 4(b).

After discussing the cavity spectra and sensitivities for the persistent current, in what follows, we present a detailed behavior of these quantities for the situation when we have the presence of the superposition of two persistent current states.

2. Two-state superposition

As our method allows us to detect both the magnitude and sign of the winding number associated with the persistent current, in this section we illustrate the capability of detecting winding numbers of two counterpropagating persistent currents for two different scenarios: one having equal magnitude but opposite signs, and the other involving different magnitudes and opposite signs. For these cases, we consider the initial state as

$$\psi(\phi) = \sqrt{\frac{N}{4\pi}} (e^{iL_{p1}\phi} + e^{iL_{p2}\phi}), \quad (18)$$

which is a superposition state of two plane waves having winding numbers L_{p1} and L_{p2} , respectively.

Figure 5 shows the condensate density profile and matter-wave OAM distribution of the condensate wave function, representing the superposition of two counterpropagating persistent currents having winding numbers $L_{p1} = 1$ and $L_{p2} = -1$. The increased modulation in condensate density is expected due to the superposition involving constructive and destructive interference of the two components of the superposition. The OAM distribution shows the dominant states that correspond to $L_p = 0$ and $\pm 2\ell$, respectively, and these peaks serve as evidence for the interference between $L_{p1} = 1$ and $L_{p2} = -1$ currents. Due to this interference, the occupation of other modes is relatively high compared with Fig. 2(b).

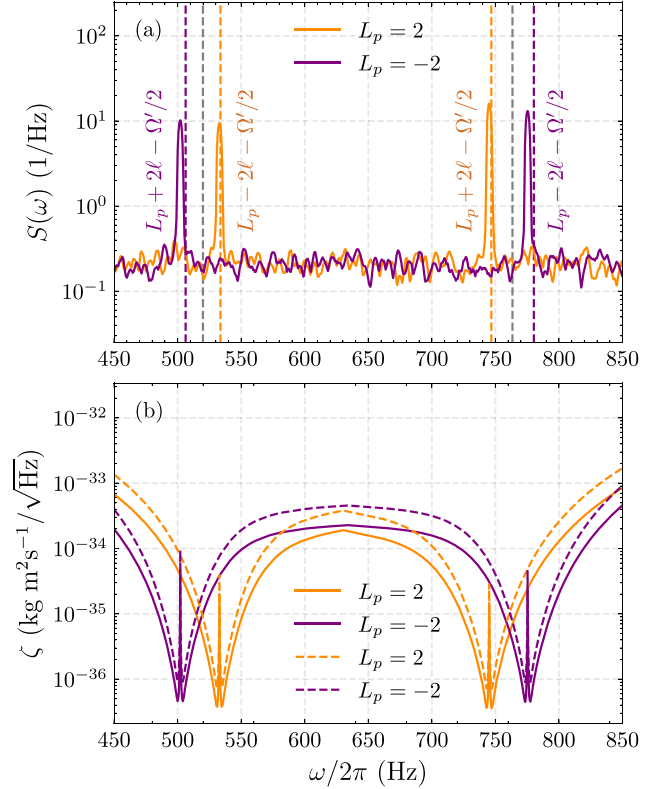


FIG. 4. Persistent current: (a) Noise spectra of the output phase quadrature of the cavity field, (b) Rotation measurement sensitivity as a function of the system response frequency for $L_p = \pm 2$. In panel (a), the gray-colored vertical dashed line corresponds to the analytical predictions for the side modes for $\Omega' = 0$ and the orange and purple-colored vertical dashed line corresponds to the analytical predictions for the side modes for $\Omega' = 0.5$. In panel (b), the solid curves correspond to ζ^Λ [Eq. (16)], while the dashed curves correspond to ζ^Ω [Eq. (17)]. Here $G = 2\pi \times 7.5$ kHz, $|\alpha_s|^2 = 0.024$, and the optomechanical measurement time (t_{meas}) is 9.4 ms. The other set of parameters used here are the same as mentioned in Fig. 2.

Figures 6(a) and 6(b) show the noise spectra of the output phase quadrature as a function of response frequency for $L_{p1} = 1, L_{p2} = -1$ and $L_{p1} = 1, L_{p2} = -2$, respectively. The peaks detected in the output spectrum represent the side mode

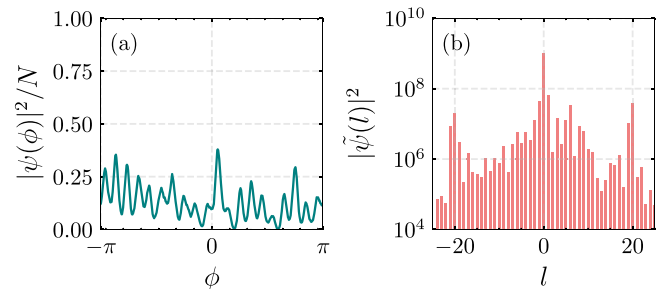


FIG. 5. Persistent current superposition: (a) Condensate density profile per particle with $L_{p1} = 1, L_{p2} = -1$, (b) OAM distribution of the condensate. Here $P_{\text{in}} = 0.7$ pW and the other parameters used are the same as in Fig. 2.

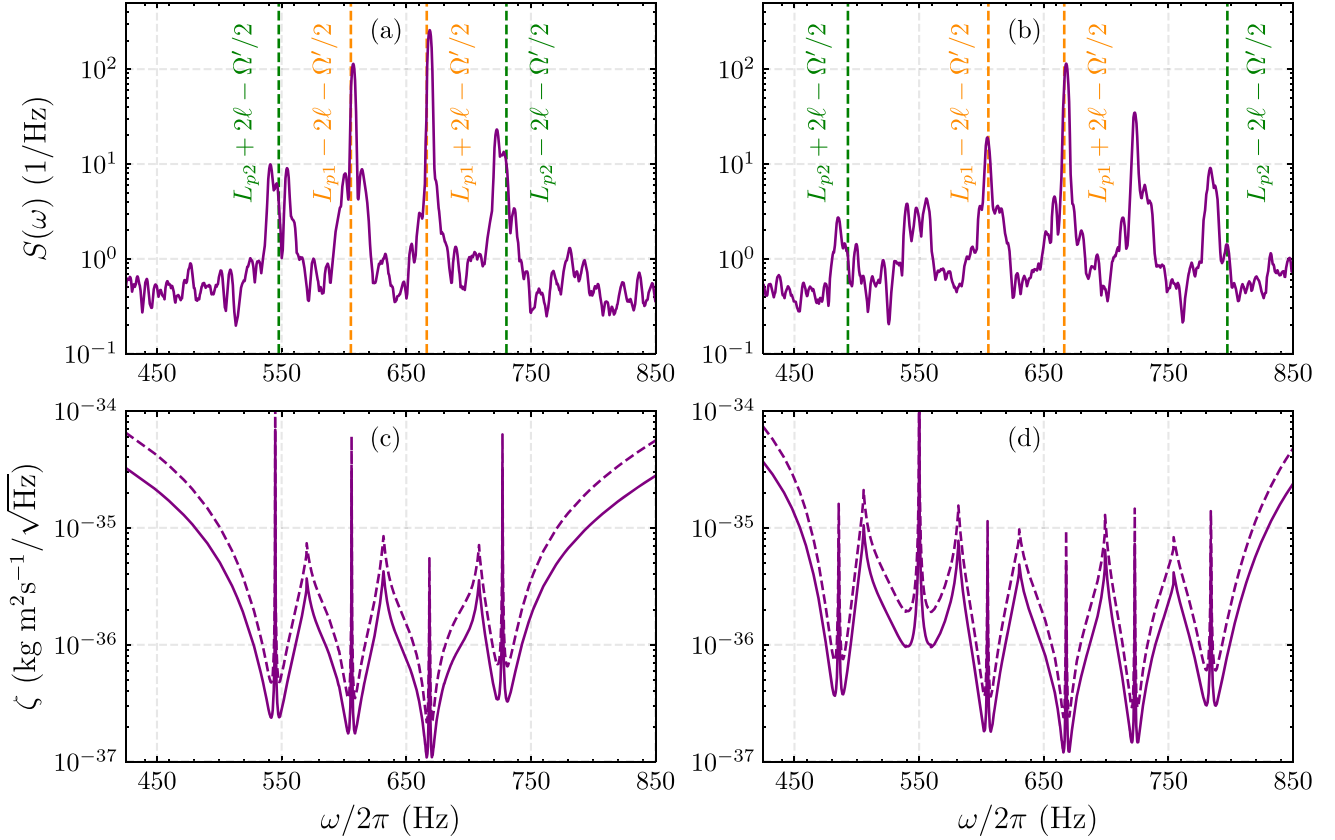


FIG. 6. Persistent current superposition: Left column for $L_{p1} = 1$ and $L_{p2} = -1$ and right column for $L_{p1} = 1$ and $L_{p2} = -2$. (a), (b) Noise spectrum of the output phase quadrature versus response frequency. (c), (d) Rotation measurement sensitivity versus response frequency. The solid curves correspond to ζ^A [Eq. (16)], while the dashed curves correspond to ζ^z [Eq. (17)]. The vertical dashed lines correspond to analytical predictions for $L_{p1} \pm 2l - \Omega'/2$ and $L_{p2} \pm 2l - \Omega'/2$. Here, $G = 2\pi \times 7.5$ kHz, $|\alpha_s|^2 = 0.33$ and the optomechanical measurement time (t_{meas}) is 2.1 ms. The other parameters used are the same as in Fig. 5.

frequencies $[\omega'_{c,d}(\Omega)]$ of the two persistent currents in the superposition state. Additionally, some extra peaks are visible, which result from the interference between these two currents. The values of the winding numbers of the constituent persistent currents were determined uniquely by locating the dominant peaks (which yield L_{p1}) and the outermost peaks (which yield L_{p2}). In implementing this procedure, careful selection of input optical power plays a pivotal role, since it not only determines the visibility of peaks in the output spectrum but also regulates the operation of the system in the linear-response regime. The increased noise in the cavity output spectra of Figs. 6(a) and 6(b), as compared with the single persistent current cases [Figs. 3(a) and 4(a)] is the consequence of employing higher input optical power. A detailed discussion on the effect of higher input optical power on the cavity output spectrum can be found in Refs. [35,61].

B. Soliton

1. Single soliton

A soliton refers to a self-bound localized state that propagates in a medium without any dispersion, and this localization is a result of the attractive interaction among the atoms constituting the soliton, as considered experimentally [62] as well as theoretically [63]. In the present work, we

study the dynamics of a matter-wave soliton forming due to the condensation of N number of ^7Li atoms having a negative scattering length, leading to an attractive interatomic interaction. In particular, we detect the rotation of this soliton in the ring trap, where the optical lattice is rotating with an angular frequency Ω . This allows us to measure the winding number associated with the soliton rotation.

For this case we first obtain the ground state as a bright soliton $[\psi_{bs}(\phi)]$ using the imaginary time scheme with an initial state as a Gaussian wave packet centered at $\phi = 0$. Following this we impart the angular motion in the bright soliton by adding a phase proportional to L_p . The resultant bright soliton will have the form as

$$\psi(\phi) = \psi_{bs}(\phi)e^{iL_p\phi}. \quad (19)$$

Figure 7(a) shows the nondispersive propagation of the bright soliton within the ring structure. The slight modulation in the density profiles of soliton can be attributed to the presence of the rotating optical lattice probe. Figure 7(b) shows the matter wave distribution of the solitonic state, and we find a pronounced concentration of OAM states close to $L_p = 1$ and $L_p \pm 2l - \Omega'/2$ (with $\Omega' = 0.5$). These multiple modes in the OAM distribution account for the complex internal dynamics of soliton. The occupancy in these states (corresponding to the side mode frequencies) is heightened in comparison to other

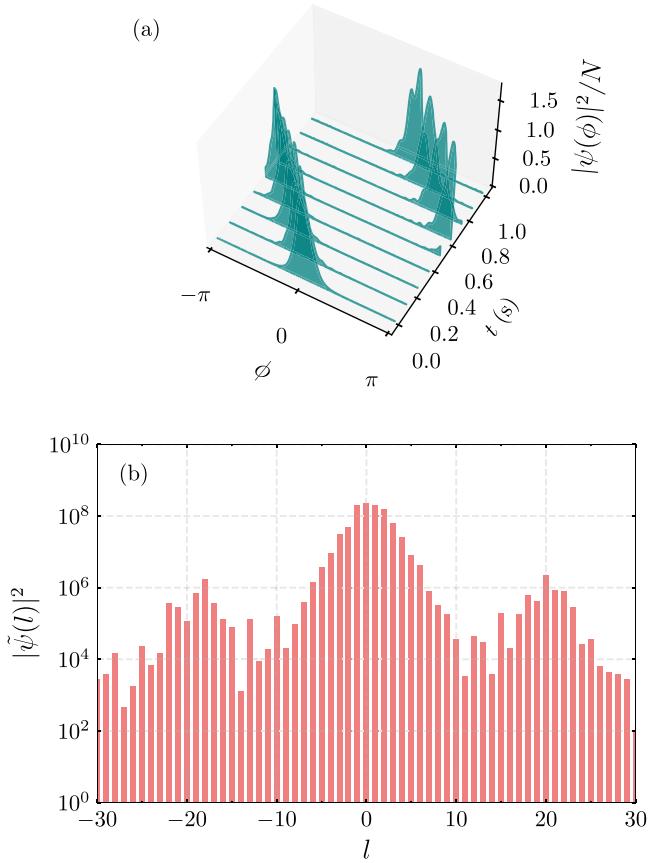


FIG. 7. Soliton: (a) Temporal evolution of density profiles of soliton, (b) OAM distribution of the soliton for $\Omega' = 0.5$, $L_p = 1$. Here $N = 6000$, $a_s = -27.6a_0$, where a_0 is the Bohr radius, $m = 7.01$ amu, and $P_{in} = 0.4$ pW, and all other parameters are same as in Fig. 2.

states [Figs. 2(b) and 5(b)], clearly indicating the occurrence of Bragg diffraction due to the presence of the optical lattice potential.

To detect the rotation of the soliton confined in the ring trap, we have calculated the noise spectra of the output phase quadrature of the cavity field for two different values of the winding number $L_p = \pm 1$ separately and have presented it as a function of the system response frequency in Fig. 8(a). The increased number of peaks in the output spectra, compared with the case of persistent current, accounts for the multimode dynamics inherent in the soliton profile. Remarkably, these two cases ($L_p = \pm 1$) yield distinct cavity output spectra, and by locating the dominating peaks in the spectrum, we can detect the sign and magnitude of the rotation of soliton in the ring. Here also, the dashed lines indicate the side mode frequencies obtained through the analytical prediction, and the numerically obtained results align closely enough with them to allow identification.

Figure 8(b) shows the rotation measurement sensitivities for the two above-discussed scenarios. We can achieve the best sensitivity to the rotation measurements near the side-mode frequencies of the condensate. Along with these, we can also get better sensitivities around the frequencies corresponding to the other neighboring modes, which was not possible

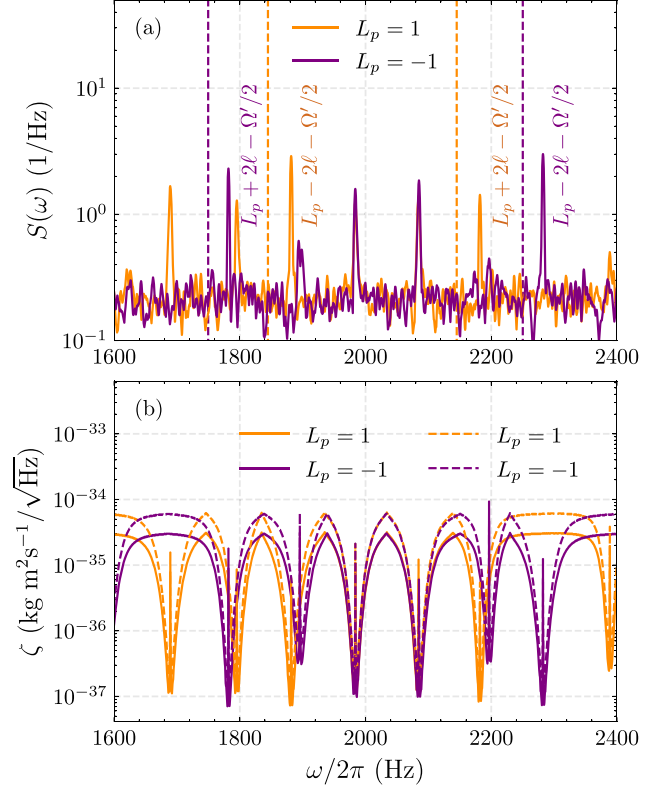


FIG. 8. Soliton: (a) Noise spectra of the output phase quadrature of the cavity field as a function of the system response frequency for $\Omega' = 0.5$, $L_p = 1$ (orange) and $L_p = -1$ (purple). The vertical dashed line corresponds to the analytical predictions for the side modes of $L_p = \pm 1$ [Eq. (6)]. (b) Rotation measurement sensitivities as a function of system response frequency. The solid curves correspond to ζ^Λ [Eq. (16)], while the dashed curves correspond to ζ^Ω [Eq. (17)]. Here $G = 2\pi \times 5.8$ kHz and $|\alpha_s|^2 = 0.192$, and the optomechanical measurement time (t_{meas}) is 6.2 ms. The other parameters used here are the same as in Fig. 7.

for the persistent current. This broader detection capability can help for a more detailed understanding of the system's behavior.

2. Collisional dynamics of counter-propagating solitons

In this section, we extend the analysis of detecting the rotation to a pair of solitons exhibiting multiple collisions [64]. These collisions depend on the effective interaction originating from the interference of two waves in the superpositioned state. We obtain the ground state of the bright soliton $[\psi_{bs}(\phi)]$ starting with the initial state as the Gaussian wave packet centered at $\phi = 0$ by implementing the imaginary time scheme. To generate the superpositioned state of the solitons we put these bright solitons centered at $-\pi/2$ and $\pi/2$ and the resultant form can be written as

$$\psi(\phi) = \psi_{bs}(\phi - \pi/2)e^{iL_p\phi} + e^{i\theta}\psi_{bs}(\phi + \pi/2)e^{iL_p\phi}. \quad (20)$$

The above equation conveys that, initially, the pair of solitons are located at $-\pi/2$ and $\pi/2$, respectively, and the specific nature of the collision is established by setting the value of phase θ between the two solitons equal to π .

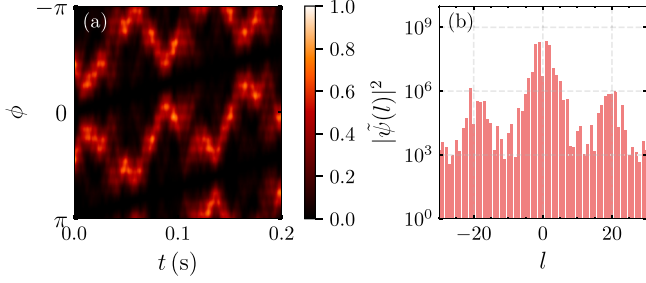


FIG. 9. Soliton collision: (a) Temporal evolution of a pair of solitons showing out-of-phase collisions, (b) OAM distribution of the solitons. Here $N = 6000$, $P_{\text{in}} = 0.4$ pW, $\Omega' = 0.3$ and other parameters used are same as Fig. 7.

Subsequently, we set up the individual soliton with distinct winding numbers $L_{p1} = -1$ and $L_{p2} = 1$, for which the solitons initially move towards each other, experiencing a repulsive collision as they move away from each other.

Figure 9(a) shows the temporal evolution of a pair of solitons exhibiting multiple collisions over time in the ring structure in the presence of a rotating optical lattice. Due to the phase difference of π between the wave packets, the interference is destructive, resulting in the formation of a zero-density point. A similar phase-dependent collision of a pair of solitons was seen in the experiment of Ref. [64]. Figure 9(b) shows the OAM distribution of the condensate containing the pair of solitons, which gives information about the side-mode generation as in earlier cases.

The noise spectrum of the phase quadrature of the cavity field is shown in Fig. 10(a). The peaks for the side modes corresponding to $L_{p1} = -1$ and $L_{p2} = 1$ are distinct and dominating, and yield information about the condensate winding number. The sensitivity of the rotation measurements is plotted in Fig. 10(b) as a function of the response frequency of the system and the best sensitivities are achieved near the side mode frequencies.

C. The ring Bose-Einstein condensate as a rotation sensor

In this section, we take the converse approach to that of our analysis above to characterize the ring BEC as a rotation sensor. We assume L_p is known for the BEC persistent current state and investigate how the magnitude and sign of Ω' can be measured. Here, Ω' now represents some unknown rotation of the laboratory that we desire to measure. As can be seen in the cavity spectra of Fig. 11 for various $\Omega' = 0.4-0.01$ for $L_p = 1$, the magnitude as well as the sign of Ω' can be determined using this technique. We find that the side-mode peaks corresponding to $\pm\Omega'$ are quite distinctly resolvable for $L_p = 1$ for $\Omega' \gtrsim 0.1$. At this point, we wish to mention that as we consider the rotation frequency above this threshold value, the rotation sensitivity comes in at about $10 \text{ mrad s}^{-1} \text{ Hz}^{-1/2}$, which is not as good as observed in the cold atom sensors, which operate at about $100 \text{ nrad s}^{-1} \text{ Hz}^{-1/2}$ [65]. This indicates a limitation of our setup as a rotation sensor.

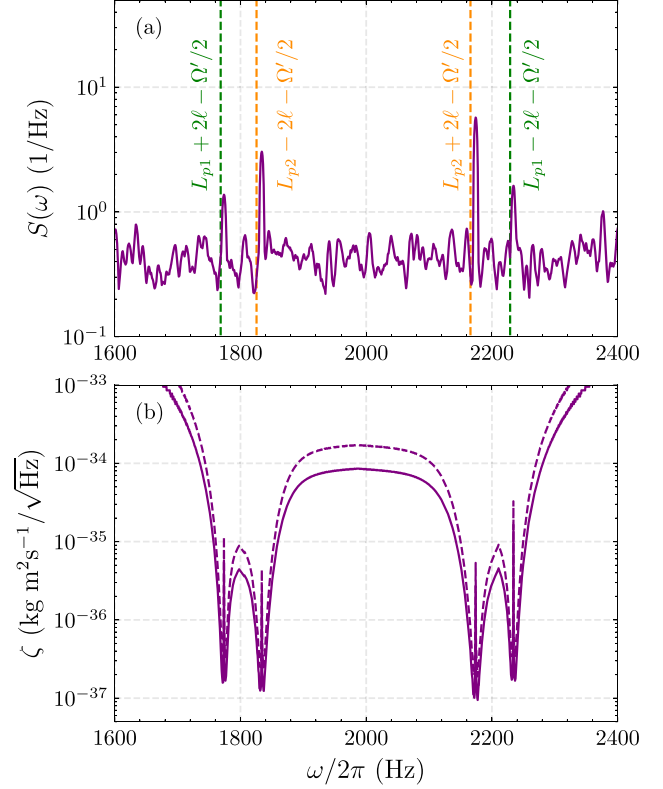


FIG. 10. Soliton collision: (a) Noise spectra of the output phase quadrature of the cavity field as a function of the system response frequency for $\Omega' = 0.3$. The dashed lines indicate the analytical predictions for the side-mode frequencies of $L_{p1} = -1$ and $L_{p2} = 1$, respectively [Eq. (6)]. (b) Rotation measurement sensitivities as a function of system response frequency. The solid curves correspond to ζ^Λ [Eq. (16)], while the dashed curves correspond to ζ^Ω [Eq. (17)]. Here $G = 2\pi \times 5.8$ kHz and $|\alpha_s|^2 = 0.192$, and the optomechanical measurement time (t_{meas}) is 6.2 ms. The other parameters used here are the same as in Fig. 9.

D. Fidelity

To demonstrate that our technique is minimally destructive and to quantify measurement backaction on the condensate [66], we have calculated the variation of fidelity of condensate wave function over time, which is defined as

$$F(t) = \int_0^{2\pi} [\psi^*(\phi, t)\psi(\phi, 0)]^2 d\phi. \quad (21)$$

Figure 12 depicts the variation of fidelity for the above-mentioned four cases. Fidelity remains close to unity for the persistent current case [Fig. 12(a)] with the slight gradual decline attributed to the measurement backaction and other noise inherent to the system. In the case of soliton [Fig. 12(c)], the fidelity shows oscillatory behavior with time, and this is linked to the rotational motion of the soliton in the ring, particularly when the soliton's spatial position deviates from its initial state. So a meaningful calculation of fidelity occurs only at those times when the soliton realigns with the initial state, characterized by a similar density and phase distribution. At these specific times (represented by the dots), the fidelity stays

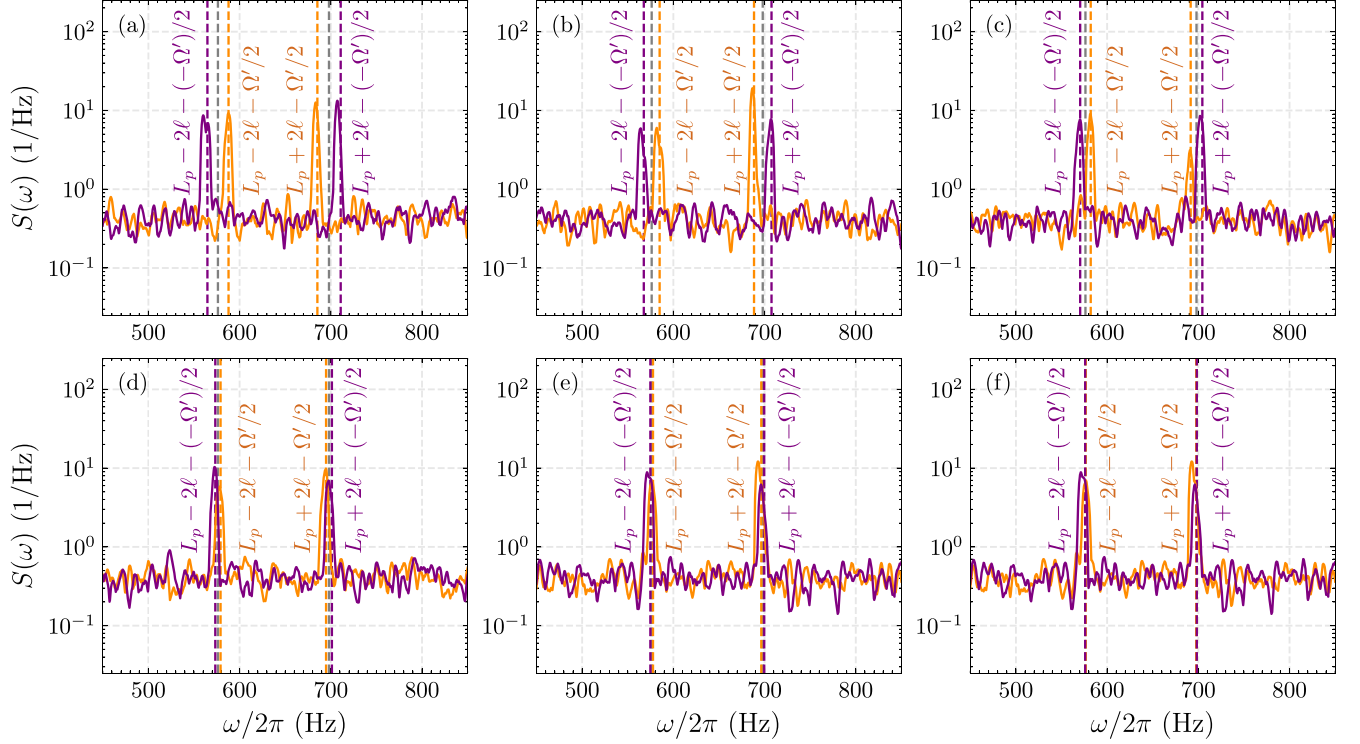


FIG. 11. Persistent current: Noise spectra of the output phase quadrature of the cavity field with $L_p = 1$ for different lattice rotation. (a) $\Omega' = 0.4$, (b) $\Omega' = 0.3$, (c) $\Omega' = 0.2$, (d) $\Omega' = 0.1$, (e) $\Omega' = 0.05$, and (f) $\Omega' = 0.01$. The gray-colored vertical dashed line corresponds to the analytical predictions for the side modes for $\Omega' = 0$ and the orange and purple-colored vertical dashed lines correspond to the analytical predictions for the side modes corresponding to the nonzero value of Ω' with $L_p = 1$ [Eq. (6)]. The other parameters used here are the same as mentioned in Fig. 2.

close to unity, which confirms that our method is minimally destructive.

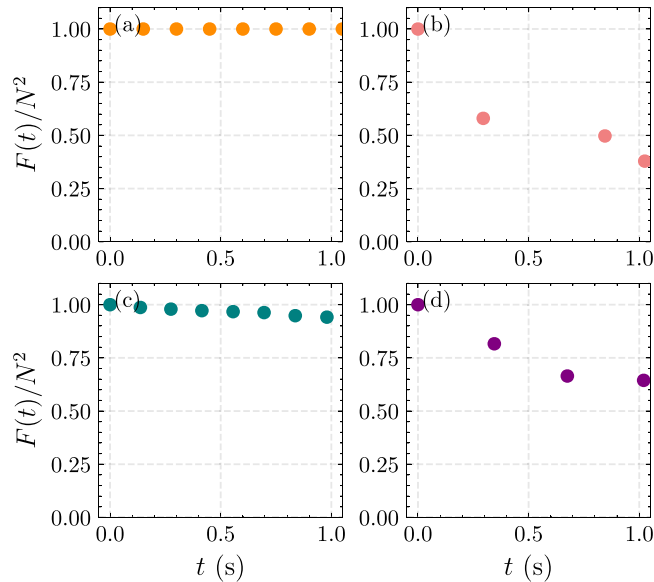


FIG. 12. Variation of fidelity with time for (a) persistent current, (b) two-state superposition of persistent current, (c) soliton, and (d) a pair of solitons. The parameters used are the same as Fig. 2 for panels (a) and (b) and Fig. 7 for panels (c) and (d).

A similar variation of fidelity emerges in the case of the superposition of persistent currents [Fig. 12(b)] and the pair of solitons [Fig. 12(d)]. However, along with the effect of the rotation, the superpositioned states are more prone to noise, as a result, the interference pattern becomes complicated. Due to this, the fidelity decreases gradually with time and the best fidelity observed, represented by the dots is near to 0.5 up to 1 s. It should be noted that this decrease in fidelity does not imply that our method is totally destructive, which is the case for the absorption imaging technique, used in demonstrated experiments so far, for the detection of rotation [1,6,7,10,20,28].

IV. SUMMARY AND CONCLUSIONS

We have theoretically considered minimally destructive, *in situ*, and real-time measurement of ring BEC rotation by coupling it to a cavity-carrying optical OAM. Unlike our previous proposal [34,35], which could only determine the magnitude and not the sign of the rotation, our present work enables the detection of both quantities. This is accomplished by rotating the optical lattice arising from the interference of the optical beams in the cavity.

We have analyzed the system using a few quantized light-matter modes as well as a mean-field (for the condensate) and classical (for the electromagnetic field) model. We have demonstrated the lattice rotation technique on persistent current rotational eigenstates, counter-rotating superpositions,

and a soliton singly or in collision with a second soliton. Our conclusions are evinced by numerical simulations of condensate density profiles (which characterize the measurement fidelity) and OAM content, optical transmission spectra from the cavity, and measurement sensitivities for condensate as well as lattice rotation as a function of the system response frequency. We find that the proposed technique can clearly distinguish between co- and counter-rotating excitations on the ring condensate. The predictions of the few-mode and multimode models are in good agreement with each other. We have also found the critical lattice rotation frequency above which our proposed technique is clearly able to lattice rotation, indicating the use of the ring BEC as a rotation sensor.

We expect the technique proposed by us to be of interest in the context of a wide class of experiments where the measurement of ring condensate rotation is of interest, such as superfluid hydrodynamics, atomtronics, and soliton interferometry, as well as for rotation sensing.

ACKNOWLEDGMENTS

We thank the International Centre for Theoretical Sciences, Bengaluru, where this work was initiated, for hosting us. M.B. would like to thank the Air Force Office of Scientific Research (FA9550-23-1-0259) for support. R.K. acknowledges support from JSPS KAKENHI Grant No. JP21K03421. P.K. acknowledges the financial support from the Max Planck Society. We also gratefully acknowledge our supercomputing facility Param-Ishan (IITG), where all the simulation runs were performed.

APPENDIX A: MEASUREMENT NOISE

In this Appendix we emphasize the nature of the measurement proposed in this paper, its concomitant noise, and its context with reference to our earlier work on the same system. First, we note that minimally destructive real-time measurement of the density dynamics of a BEC by observation of the cavity optical output is an established experimental procedure [36,67]. In these experiments the fundamental noise consists of the shot noise of the measuring optical field, quantum backaction which can be understood as the disturbance caused to the condensate by the laser shot noise, leading to degradation of optical phase readout precision at high cavity driving powers [37], intrinsic condensate quantum fluctuations, and thermal noise due to the nonzero temperature of the BEC. In these works, the theoretical framework typically consists of a few-mode (the cavity optical mode plus the matter wave linear momentum side modes) quantum-mechanical model, which show good agreement with the experimental data. The measurement quantum backaction can be calculated from such models.

Second, in our previous work following the similar line of the above-mentioned work in the ring BEC in a cavity [34], we proposed a few mode quantum model. There, along with other noise effects, we calculated the quantum backaction and indicated how the measurement can be made minimally destructive by operating at the standard quantum limit [37]. Further we computed the measurement time t_{meas} and systematically showed it to be much smaller than the timescales

associated with persistent current flow, thus making the measurement practically real time.

Third, for our present model, we consider all—rather than few—of the modes of the condensate on the ring. As we regard the dynamics of the condensate in the mean-field approximation, we wish to mention two important points of our model. First, taking the mean-field limit only means that the quantum *correlations* in the condensate are neglected. However, each atom in the condensate is still treated quantum mechanically. The function $\psi(\phi, \tau)$ which solves our nonlinear Schrödinger equation of Eq. (7), is the condensate *wave function*, a quantum-mechanical object [68]. We emphasize that $\psi(\phi, \tau)$ is quantum in nature because it describes the single-particle wave function of each atom in the condensate, and only in the quantum-mechanical regime can a single atom be described as a wave. Second, we note that the occurrence of backaction does not require the presence of correlations—even a single atom can experience backaction.

Putting together all the observations made above, we find our mean-field equations [Eqs. (7) and (8)] incorporate all relevant sources of noise in the following way. The shot noise in the measuring laser is modeled by α_{in} . It couples in to the intracavity field α via Eq. (8). This noisy field α then disturbs (couples to) the condensate wave function ψ through the second term on the right-hand side of Eq. (7). The perturbed condensate wave function adds noise back to the cavity field α through the expectation value $\langle \cos^2(\ell\phi) \rangle_{\tau}$ in Eq. (8). Finally, through the input-output relation $\alpha_{\text{out}} = -\alpha_{\text{in}} + \sqrt{\gamma_0}\alpha$, the cavity output α_{out} picks up this noise from the cavity mode α , thus leading to degradation of phase readout precision at high optical powers, which is the effect of quantum backaction in optomechanics [37]. The intrinsic fluctuations of the condensate variables are contained in $\psi(\phi, \tau)$ and the effects of nonzero temperature are represented by $\xi(\phi, \tau)$ in Eq. (7). Thus, our mean-field model contains all sources of noise relevant to the measurement [66].

APPENDIX B: CHIRALITY DETECTION AND ROTATION SENSING AT HIGH ROTATION RATE OF OPTICAL LATTICE

In this Appendix, we present the simulation results pertaining to the chirality detection and rotational sensitivity measurement for the situation when the condensate is subject to high rotation along with the optical trap.

1. Persistent current

The corresponding results for persistent current are shown in Figs. 13(a)–13(c) depicts the condensate density profiles for increasing the rotation frequency of the optical lattice for $L_p = 1$. We note that for $\Omega' = 2L_p$, the side mode frequencies $\omega'_c \equiv \omega'_d = \pm 2\ell$ [Fig. 13(b)]. The corresponding OAM distributions are presented in Figs. 13(d)–13(f). When $\Omega' = 2$ for $L_p = 1$ [Fig. 13(e)], the occupancies of the $L_p \pm 2\ell$ modes are nearly equal and decreased by an order of magnitude from the other cases.

Figures 13(g)–13(i) show the noise spectra of the phase quadrature of the cavity transmission for the above-mentioned

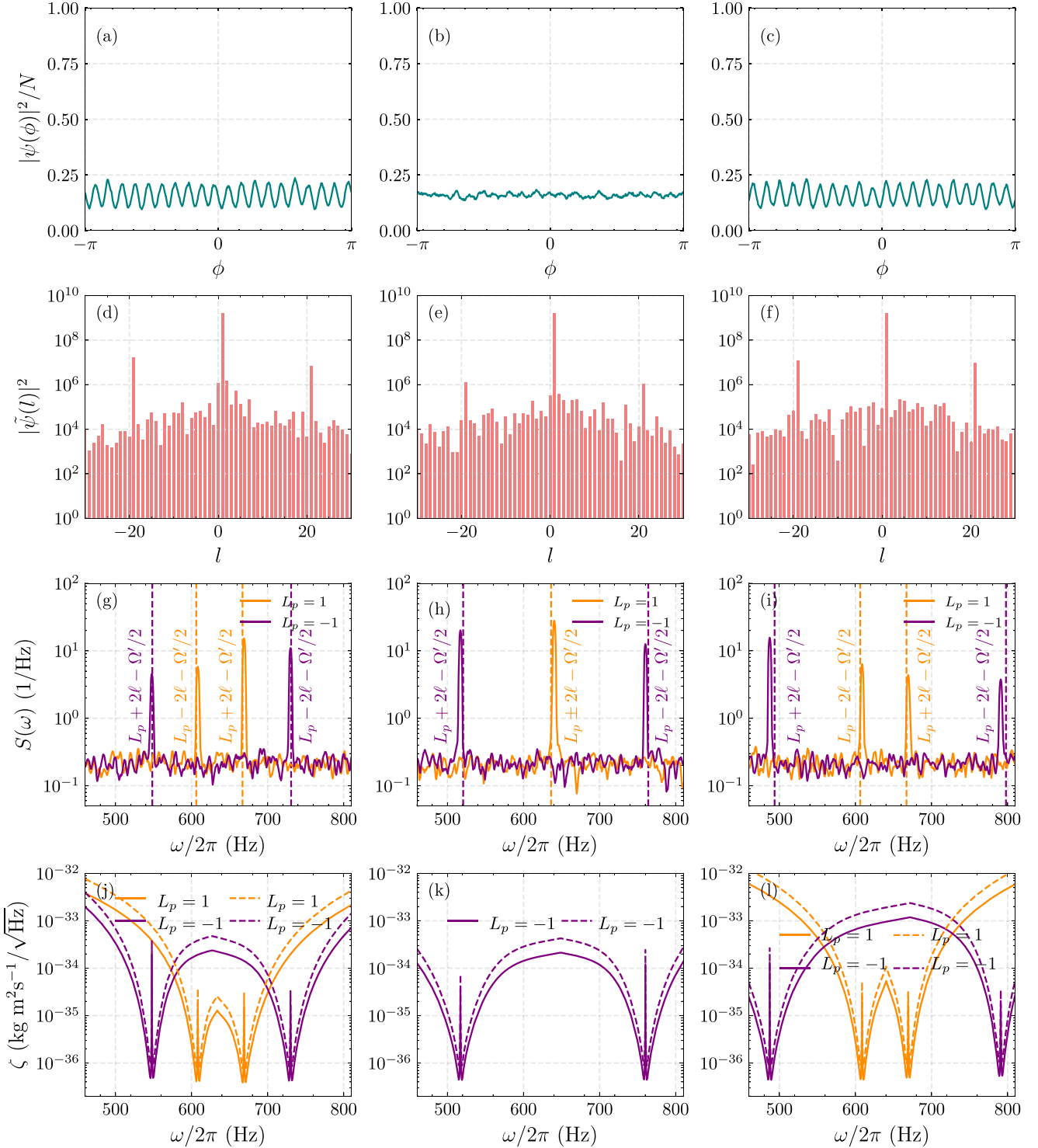


FIG. 13. Persistent current: [(a)–(c)] Density profiles of persistent current for $L_p = 1$. [(d)–(f)] OAM states of the condensate for $L_p = 1$. [(g)–(i)] Noise spectrum of the output phase quadrature versus response frequency. The vertical dashed line corresponds to the analytical predictions for the side modes (colors are used in the same way as in Fig. 3). [(j)–(l)] Rotation measurement sensitivity as a function of system response frequency. The solid curves correspond to ζ^Λ [Eq. (16)], while the dashed curves correspond to ζ^Ω [Eq. (17)]. Here $P_{\text{in}} = 50$ fW and $\Omega' = 1, 2$, and 3 respectively. The remaining set of parameters are the same as in Fig. 2.

three cases $\Omega' = 1, 2$, and 3, respectively. When $\Omega'/2 \neq L_p$, we get distinct peaks for $L_p = 1$ and $L_p = -1$ and the information about the winding number can be detected. Otherwise, we obtain a single degenerate peak in the output spectrum

(when $\Omega'/2 = L_p$) and by using this relation between Ω' and L_p , the magnitude and sign of the winding number of the persistent current can be obtained. The corresponding rotation measurement sensitivities are shown in Figs. 13(j)–13(l) and

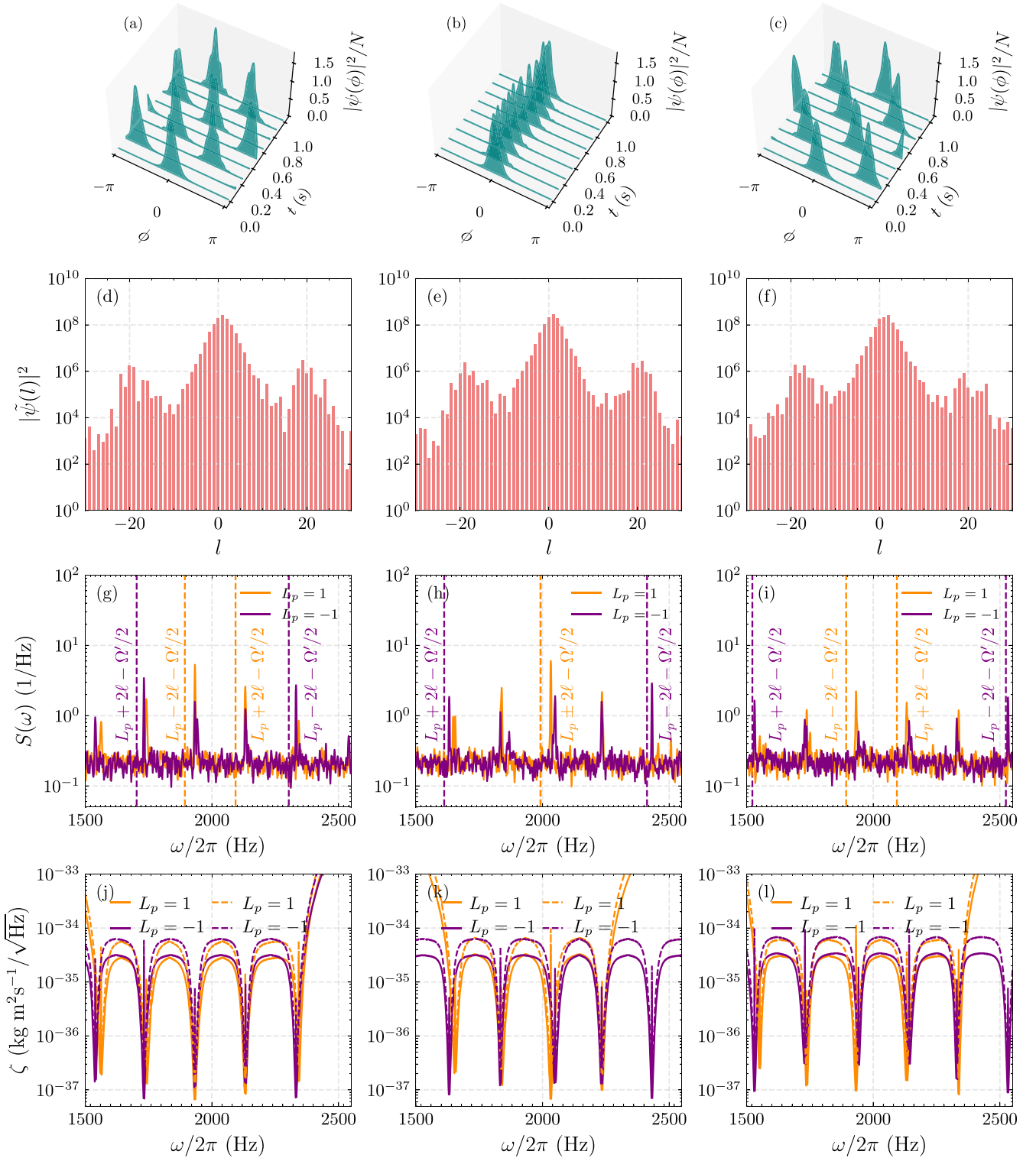


FIG. 14. Soliton: [(a)–(c)] Density profiles of soliton for $L_p = 1$. [(d)–(f)] OAM states of the condensate for $L_p = 1$. [(g)–(i)] Power spectrum of the imaginary part of cavity field versus response frequency. The vertical dashed line corresponds to the analytical predictions for the side modes (colors are used in the same way as in Fig. 3). [(j)–(l)] Rotation measurement sensitivities as a function of system response frequency. The solid curves correspond to ζ^Λ [Eq. (16)], while the dashed curves correspond to ζ^Ω [Eq. (17)]. Here $P_{\text{in}} = 0.4 \text{ pW}$ and $\Omega' = 1, 2, \text{ and } 3$ respectively. The remaining set of parameters are the same as in Fig. 7.

the best sensitivities are obtained near the side mode frequencies as in earlier cases.

2. Soliton

The rotation of soliton in the ring structure is presented in Figs. 14(a)–14(c), corresponding to $\Omega' = 1, 2,$ and $3,$ respectively, and the corresponding orbital

angular-momentum distribution are shown in Figs. 14(d)–14(f). The noise spectra of the phase quadrature of the cavity field for these three cases are shown in Figs. 14(g)–14(i), respectively. Due to the multimode nature of the soliton, a larger number of peaks is observed, as discussed earlier in Sec. III B; nonetheless, by locating and measuring the dominating peaks, the information about the winding number can be extracted accurately.

-
- [1] C. Ryu, M. F. Andersen, P. Cladé, V. Natarajan, K. Helmerson, and W. D. Phillips, Observation of persistent flow of a Bose-Einstein condensate in a toroidal trap, *Phys. Rev. Lett.* **99**, 260401 (2007).
- [2] Y. Guo, R. Dubessy, M. d. G. de Herve, A. Kumar, T. Badr, A. Perrin, L. Longchambon, and H. Perrin, Supersonic rotation of a superfluid: A long-lived dynamical ring, *Phys. Rev. Lett.* **124**, 025301 (2020).
- [3] Y. Cai, D. G. Allman, P. Sabharwal, and K. C. Wright, Persistent currents in rings of ultracold fermionic atoms, *Phys. Rev. Lett.* **128**, 150401 (2022).
- [4] G. Del Pace, K. Xhani, A. Muzi Falconi, M. Fedrizzi, N. Grani, D. Hernandez Rajkov, M. Inguscio, F. Scazza, W. J. Kwon, and G. Roati, Imprinting persistent currents in tunable fermionic rings, *Phys. Rev. X* **12**, 041037 (2022).
- [5] Y. Guo, E. M. Gutierrez, D. Rey, T. Badr, T. Perrin, L. Longchambon, V. S. Bagnato, H. Perrin, and R. Dubessy, Expansion of a quantum gas in a shell trap, *New J. Phys.* **24**, 093040 (2022).
- [6] S. Moulder, S. Beattie, R. P. Smith, N. Tammuz, and Z. Hadzibabic, Quantized supercurrent decay in an annular Bose-Einstein condensate, *Phys. Rev. A* **86**, 013629 (2012).
- [7] K. C. Wright, R. B. Blakestad, C. J. Lobb, W. D. Phillips, and G. K. Campbell, Driving phase slips in a superfluid atom circuit with a rotating weak link, *Phys. Rev. Lett.* **110**, 025302 (2013).
- [8] K. Snizhko, K. Isaieva, Y. Kuriatnikov, Y. Bidasyuk, S. Vilchinskii, and A. Yakimenko, Stochastic phase slips in toroidal Bose-Einstein condensates, *Phys. Rev. A* **94**, 063642 (2016).
- [9] R. Kanamoto, H. Saito, and M. Ueda, Stability of the quantized circulation of an attractive Bose-Einstein condensate in a rotating torus, *Phys. Rev. A* **68**, 043619 (2003).
- [10] S. Eckel, J. Lee, F. Jendrzejewski, N. Murray, C. W. Clark, C. J. Lobb, W. D. Phillips, M. Edwards, and G. K. Campbell, Hysteresis in a quantized superfluid ‘atomtronic’ circuit, *Nature (London)* **506**, 200 (2014).
- [11] J. Hou, X.-W. Luo, K. Sun, and C. Zhang, Adiabatically tuning quantized supercurrents in an annular Bose-Einstein condensate, *Phys. Rev. A* **96**, 011603(R) (2017).
- [12] K. C. Wright, R. B. Blakestad, C. J. Lobb, W. D. Phillips, and G. K. Campbell, Threshold for creating excitations in a stirred superfluid ring, *Phys. Rev. A* **88**, 063633 (2013).
- [13] S. Beattie, S. Moulder, R. J. Fletcher, and Z. Hadzibabic, Persistent currents in spinor condensates, *Phys. Rev. Lett.* **110**, 025301 (2013).
- [14] A. Gallemí, A. M. Mateo, R. Mayol, and M. Guilleumas, Coherent quantum phase slip in two-component bosonic atomtronic circuits, *New J. Phys.* **18**, 015003 (2015).
- [15] Y. H. Wang, A. Kumar, F. Jendrzejewski, R. M. Wilson, M. Edwards, S. Eckel, G. K. Campbell, and C. W. Clark, Resonant wavepackets and shock waves in an atomtronic SQUID, *New J. Phys.* **17**, 125012 (2015).
- [16] R. Kanamoto, L. D. Carr, and M. Ueda, Topological winding and unwinding in metastable Bose-Einstein condensates, *Phys. Rev. Lett.* **100**, 060401 (2008).
- [17] A. Das, J. Sabbatini, and W. H. Zurek, Winding up superfluid in a torus via Bose Einstein condensation, *Sci. Rep.* **2**, 352 (2012).
- [18] L. Corman, L. Chomaz, T. Bienaimé, R. Desbuquois, C. Weitenberg, S. Nascimbène, J. Dalibard, and J. Beugnon, Quench-induced supercurrents in an annular Bose gas, *Phys. Rev. Lett.* **113**, 135302 (2014).
- [19] I. Yatsuta, B. Malomed, and A. Yakimenko, Acoustic analog of Hawking radiation in quantized circular superflows of Bose-Einstein condensates, *Phys. Rev. Res.* **2**, 043065 (2020).
- [20] S. Eckel, A. Kumar, T. Jacobson, I. B. Spielman, and G. K. Campbell, A rapidly expanding Bose-Einstein condensate: An expanding universe in the lab, *Phys. Rev. X* **8**, 021021 (2018).
- [21] P. Öhberg and E. M. Wright, Quantum time crystals and interacting gauge theories in atomic Bose-Einstein condensates, *Phys. Rev. Lett.* **123**, 250402 (2019).
- [22] S. Gupta, K. W. Murch, K. L. Moore, T. P. Purdy, and D. M. Stamper-Kurn, Bose-Einstein condensation in a circular waveguide, *Phys. Rev. Lett.* **95**, 143201 (2005).
- [23] G. E. Marti, R. Olf, and D. M. Stamper-Kurn, Collective excitation interferometry with a toroidal Bose-Einstein condensate, *Phys. Rev. A* **91**, 013602 (2015).
- [24] J. J. Cooper, D. W. Hallwood, and J. A. Dunningham, Entanglement-enhanced atomic gyroscope, *Phys. Rev. A* **81**, 043624 (2010).
- [25] G. Pelegrí, J. Mompart, and V. Ahufinger, Quantum sensing using imbalanced counter-rotating Bose-Einstein condensate modes, *New J. Phys.* **20**, 103001 (2018).
- [26] A. Ramanathan, K. C. Wright, S. R. Muniz, M. Zelan, W. T. Hill, C. J. Lobb, K. Helmerson, W. D. Phillips, and G. K. Campbell, Superflow in a toroidal Bose-Einstein condensate: An atom circuit with a tunable weak link, *Phys. Rev. Lett.* **106**, 130401 (2011).
- [27] C. Ryu, P. W. Blackburn, A. A. Blinova, and M. G. Boshier, Experimental realization of Josephson junctions for an atom SQUID, *Phys. Rev. Lett.* **111**, 205301 (2013).
- [28] S. Pandey, H. Mas, G. Vasilakis, and W. von Klitzing, Atomtronic matter-wave lensing, *Phys. Rev. Lett.* **126**, 170402 (2021).
- [29] L. Amico, D. Anderson, M. Boshier, J.-P. Brantut, L.-C. Kwek, A. Minguzzi, and W. von Klitzing, Colloquium: Atomtronic circuits: From many-body physics to quantum technologies, *Rev. Mod. Phys.* **94**, 041001 (2022).
- [30] D. Aghamalyan, M. Cominotti, M. Rizzi, D. Rossini, F. Hekking, A. Minguzzi, L.-C. Kwek, and L. Amico, Coherent

- superposition of current flows in an atomtronic quantum interference device, *New J. Phys.* **17**, 045023 (2015).
- [31] S. Ragole and J. M. Taylor, Interacting atomic interferometry for rotation sensing approaching the Heisenberg limit, *Phys. Rev. Lett.* **117**, 203002 (2016).
- [32] N. Murray, M. Krygier, M. Edwards, K. C. Wright, G. K. Campbell, and C. W. Clark, Probing the circulation of ring-shaped Bose-Einstein condensates, *Phys. Rev. A* **88**, 053615 (2013).
- [33] A. Kumar, N. Anderson, W. D. Phillips, S. Eckel, G. K. Campbell, and S. Stringari, Minimally destructive, Doppler measurement of a quantized flow in a ring-shaped Bose-Einstein condensate, *New J. Phys.* **18**, 025001 (2016).
- [34] P. Kumar, T. Biswas, K. Feliz, R. Kanamoto, M.-S. Chang, A. K. Jha, and M. Bhattacharya, Cavity optomechanical sensing and manipulation of an atomic persistent current, *Phys. Rev. Lett.* **127**, 113601 (2021).
- [35] N. Pradhan, P. Kumar, R. Kanamoto, T. N. Dey, M. Bhattacharya, and P. K. Mishra, Cavity optomechanical detection of persistent currents and solitons in a bosonic ring condensate, *Phys. Rev. Res.* **6**, 013104 (2024).
- [36] F. Brennecke, S. Ritter, T. Donner, and T. Esslinger, Cavity optomechanics with a Bose-Einstein condensate, *Science* **322**, 235 (2008).
- [37] M. Aspelmeyer, T. J. Kippenberg, and F. Marquardt, Cavity optomechanics, *Rev. Mod. Phys.* **86**, 1391 (2014).
- [38] B. P. Abbott *et al.* (LIGO Scientific Collaboration and Virgo Collaboration), Observation of gravitational waves from a binary black hole merger, *Phys. Rev. Lett.* **116**, 061102 (2016).
- [39] X. He, P. Xu, J. Wang, and M. Zhan, Rotating single atoms in a ring lattice generated by a spatial light modulator, *Opt. Express* **17**, 21007 (2009).
- [40] J. Brand and W. P. Reinhardt, Generating ring currents, solitons and vortices by stirring a Bose-Einstein condensate in a toroidal trap, *J. Phys. B: At., Mol. Opt. Phys.* **34**, L113 (2001).
- [41] G. M. Kavoulakis, Bose-Einstein condensates with attractive interactions on a ring, *Phys. Rev. A* **67**, 011601(R) (2003).
- [42] L. A. Toikka, O. Kärki, and K.-A. Suominen, Creation and revival of ring dark solitons in an annular Bose-Einstein condensate, *J. Phys. B: At., Mol. Opt. Phys.* **47**, 021002 (2014).
- [43] G. D. McDonald, C. C. N. Kuhn, K. S. Hardman, S. Bennetts, P. J. Everitt, P. A. Altin, J. E. Debs, J. D. Close, and N. P. Robins, Bright solitonic matter-wave interferometer, *Phys. Rev. Lett.* **113**, 013002 (2014).
- [44] J. L. Helm, S. L. Cornish, and S. A. Gardiner, Sagnac interferometry using bright matter-wave solitons, *Phys. Rev. Lett.* **114**, 134101 (2015).
- [45] D. Gallucci and N. P. Proukakis, Engineering dark solitary waves in ring-trap Bose-Einstein condensates, *New J. Phys.* **18**, 025004 (2016).
- [46] D. M. Jezek, P. Capuzzi, and H. M. Cataldo, Dark-soliton collisions in a toroidal Bose-Einstein condensate, *Phys. Rev. A* **93**, 023601 (2016).
- [47] H. Cataldo and D. M. Jezek, Collisional dynamics of multiple dark solitons in a toroidal Bose-Einstein condensate: Quasiparticle picture, *Eur. Phys. J. D* **72**, 213 (2018).
- [48] S. Safaei, L.-C. Kwek, R. Dumke, and L. Amico, Monitoring currents in cold-atom circuits, *Phys. Rev. A* **100**, 013621 (2019).
- [49] M. Kolář, T. Opatrný, and K. K. Das, Criticality and spin squeezing in the rotational dynamics of a Bose-Einstein condensate on a ring lattice, *Phys. Rev. A* **92**, 043630 (2015).
- [50] H. Huang and K. K. Das, Effects of a rotating periodic lattice on coherent quantum states in a ring topology: The case of positive nonlinearity, *Phys. Rev. A* **104**, 053320 (2021).
- [51] S. Ritter, F. Brennecke, K. Baumann, T. Donner, C. Guerlin, and T. Esslinger, Dynamical coupling between a Bose-Einstein condensate and a cavity optical lattice, *Appl. Phys. B: Lasers Opt.* **95**, 213 (2009).
- [52] Y. Lim, Y. Lee, J. Goo, D. Bae, and Y. Shin, Vortex shedding frequency of a moving obstacle in a Bose-Einstein condensate, *New J. Phys.* **24**, 083020 (2022).
- [53] H. T. Stoof, Coherent versus incoherent dynamics during Bose-Einstein condensation in atomic gases, *J. Low Temp. Phys.* **114**, 11 (1999).
- [54] H. Stoof and M. Bijlsma, Dynamics of fluctuating Bose-Einstein condensates, *J. Low Temp. Phys.* **124**, 431 (2001).
- [55] R. Kubo, The fluctuation-dissipation theorem, *Rep. Prog. Phys.* **29**, 255 (1966).
- [56] T. Mithun, S. C. Ganguli, P. Raychaudhuri, and B. Dey, Signatures of two-step impurity-mediated vortex lattice melting in Bose-Einstein condensates, *Europhys. Lett.* **123**, 20004 (2018).
- [57] D. Dutykh, A brief introduction to pseudo-spectral methods: Application to diffusion problems, [arXiv:1606.05432](https://arxiv.org/abs/1606.05432).
- [58] D. Tan and Z. Chen, On a general formula of fourth order Runge-Kutta method, *J. Math. Sci. Math. Educ.* **7**, 1 (2012).
- [59] W. Bao, D. Jaksch, and P. A. Markowich, Numerical solution of the Gross-Pitaevskii equation for Bose-Einstein condensation, *J. Comput. Phys.* **187**, 318 (2003).
- [60] D. Naidoo, K. Ait-Ameur, M. Brunel, and A. Forbes, Observation of superfluid flow in a Bose-Einstein condensed gas, *Appl. Phys. B: Lasers Opt.* **106**, 683 (2012).
- [61] M. Bhattacharya, Rotational cavity optomechanics, *J. Opt. Soc. Am. B* **32**, B55 (2015).
- [62] U. Al Khawaja, H. T. C. Stoof, R. G. Hulet, K. E. Strecker, and G. B. Partridge, Bright soliton trains of trapped Bose-Einstein condensates, *Phys. Rev. Lett.* **89**, 200404 (2002).
- [63] S. Gangwar, R. Ravisankar, P. Muruganandam, and P. K. Mishra, Dynamics of quantum solitons in Lee-Huang-Yang spin-orbit-coupled Bose-Einstein condensates, *Phys. Rev. A* **106**, 063315 (2022).
- [64] J. H. Nguyen, P. Dyke, D. Luo, B. A. Malomed, and R. G. Hulet, Collisions of matter-wave solitons, *Nat. Phys.* **10**, 918 (2014).
- [65] I. Dutta, D. Savoie, B. Fang, B. Venon, C. L. Garrido Alzar, R. Geiger, and A. Landragin, Continuous cold-atom inertial sensor with 1 nrad/sec rotation stability, *Phys. Rev. Lett.* **116**, 183003 (2016).
- [66] E. P. Yamaguchi, H. M. Hurst, and I. B. Spielman, Feedback-cooled Bose-Einstein condensation: Near and far from equilibrium, *Phys. Rev. A* **107**, 063306 (2023).
- [67] F. Brennecke, R. Mottl, K. Baumann, R. Landig, T. Donner, and T. Esslinger, Real-time observation of fluctuations at the driven-dissipative Dicke phase transition, *Proc. Natl. Acad. Sci. USA* **110**, 11763 (2013).
- [68] C. J. Pethick and H. Smith, *Bose-Einstein Condensation in Dilute Gases* (Cambridge University Press, Cambridge, UK, 2008).